Impact of proportional resonant controller parameters of VSC connected to AC grids with variable X/R characteristic on the small signal stability

Marta Haro-Larrode[a,b,*], Maider Santos-Mugica[a], Pablo Eguia[b], Raul Rodriguez-Sanchez[a], Asier Gil-de-Muro[a]

[a] Tecnalia Research and Innovation, Astondo bidea, Edificio 700, 48160 Derio, Spain
[b] University of The Basque Country (UPV), Department of Electrical Engineering, Alameda Urquijo s/n, 48013 Bilbao, Spain

ARTICLE INFO

Keywords:
VSC
Small signal
AC grid strength
Proportional-resonant controller
Modal analysis

ABSTRACT

The purpose of this paper is to assess the impact of proportional resonant controller (*PR*) parameters of a Voltage Source Converter (*VSC*) and AC grid topology on the small signal stability of a VSC-AC system. Based on this, a small signal model is constructed, step by step, and validated against *EMT* simulations. Following this validation, several scenarios containing different *PR* controller gains are proposed and compared by means of trajectory of eigenvalues. A discussion of the best adequacy of *PR* controller parameters and AC grid strength in combination with inductive-resistive characteristic (X/R) is developed to ensure the stability of the system. The previous eigenvalue analysis is verified in time domain by means of *EMT* simulations. The analysis performed concludes that, while the AC grid strength in combination with *PR* controller parameters plays an important role in determination of stability, variations in the inductive-resistive AC grid characteristic need to be included in the analysis, since further instabilities can appear even when the PR controller is well designed for a specific AC grid configuration.

1. Introduction

Nowadays, High Voltage Direct Current (*HVDC*) transmission systems are becoming a key technology to convey great amounts of energy from remote areas to *AC* grids, as it is the case of offshore wind farms, placed in locations with high wind energy potential [1]. *HVDC* technology can be implemented with Current Source Converters (*CSC*) or with Voltage Source Converters (*VSC*). *VSC* technology presents technical advantages, such as the ability to control active and reactive power independently, provide high controllability of *DC* grid, and black start capability [2]. The control schemes of *VSC* converters usually operate in two levels: outer and inner control [3,4]. The outer controller is responsible for active and reactive power control, frequency control and other type of control services while the inner controller undertakes the responsibility for current control. Most of the inner controllers are based on Proportional Integral (*PI*) controllers [5–10] but other less common control structures, such as Proportional Resonant (*PR*) controllers [11–13], can be found in the literature.

In the last decade, *PR* controllers have appeared as an alternative to *PI* controllers, due to their unique behaviour under unbalanced operation [11]. To this effect, *PR*s operate in αβ-frame, which allows them to track both balanced and unbalanced current references and provide an improved response under unbalanced faults in comparison to the response provided by *PI* controllers. Besides, with *PR* controllers the grid current waveforms are enhanced when interface inductors are not perfectly balanced between the phases. *PR* controllers are used to overcome drawbacks that simple linear *PI* controllers have, such as the elimination of steady-state errors [11–14]. In [12] the main drawbacks of *PI* controllers, as being the presence of steady-state error in the stationary frame and the need to decouple phase dependency in 3-phase systems, are listed. Since *PI* controllers are very simple to implement, many modifications of them, such as a grid voltage feed-forward path, have been applied to increase their bandwidth but at a cost of pushing the system containing *PI* controllers and its respective plant towards its stability limits [12]. Apart from these, other benefits of stationary-frame controllers are identified in [14]. One of them is the removal of the Phase Locked Loop (*PLL*), which eliminates errors due to synchronization problems. Another advantage is the elimination of inverse Park transformations, which reduces overall computational burden. However, *PR* controllers have invariant modulation blocks in their control loop, which inhibits the use of parameterization techniques such as eigenvalue analysis. Therefore, a proper linearization of *PR* controller is

* Corresponding author.
E-mail address: marta.haro@tecnalia.com (M. Haro-Larrode).

Nomenclature

CSC	current source converter
EMT	electromagnetic transient
ENTSOE	European network of transmission system operators
f	*AC* grid frequency
f_h	frequency threshold
FSM_{th}	frequency sensitive mode y-intercept
HVDC	high voltage direct current
$I_{d,AC}$ $I_{q,AC}$	*AC* current measured in d and q coordinates
$I_{d,ref}$ $I_{q,ref}$	current setpoints in d and q coordinates
k_0	constant related to sinusoidal modulation of *VSC*
$k_{droop,AC}$	droop *AC* constant that relates reactive power with *AC* voltage in outer controller
k_{FSM}	*FSM* slope for frequency control in outer controller
k_i k_p	PR integral and proportional constants in inner proportional resonant controller, respectively
k_v k_q	proportional constant in d and q components of proportional integral in Outer controller, respectively
LFSM	limited sensitive frequency mode according to *ENTSOE*
LTI	linear time invariant
P_{aux}	DC power measured by the time a frequency deviation exceeds a threshold that activates an ancillary frequency function
PCC	point of common coupling
P_{DC}	DC power measured at HVDC cable
PI	proportional integral
PLL	phase locked loop
Pmd Pmq	modulation index in d and q coordinates
Pmd_{ss} Pmq_{ss}	modulation index in d and q coordinates in steady-state regime
PR	proportional resonant
Q_{AC} $Q_{AC,ref}$	reactive power measured and setpoint in outer controller, respectively
Q_{droop}	droop reactive function
R,L	*AC* line resistance and inductance
R_f, L_f	output filter resistance and inductance of the VSC
SCR	short circuit ratio
T_v T_q	time constant in d and q components of PI in outer controller
V_{AC} $V_{AC,ref}$	*AC* voltage module magnitude measured and setpoint at the VSC *AC* output
$V_{d,AC}$ $V_{q,AC}$	*AC* voltage in d and q coordinates at the VSC output
$V_{d,PCC}$ $V_{q,PCC}$	*AC* voltage measured at the PCC in d and q coordinate
$V_{d,ref}$ $V_{q,ref}$	output voltage of PR controller in d and q coordinates
$V_{d,ref,ss}$ $V_{q,ref,ss}$	output voltage of PR controller in d and q coordinates in steady-state regime
V_{DC} $V_{DC,ref}$	DC voltage measured and setpoint at the DC side of VSC
$V_{DC,diff}$	mean value of the positive and negative DC voltage measurents
$V_{DC,diff,ss}$	mean value of the positive and negative DC voltage measurents in steady-state regime
$V_{DC,ss}$	DC voltage in steady-state regime
V_{DC}^{+} V_{DC}^{-}	positive and negative DC voltages measured at each pole of the HVDC link
VSC	Voltage Source Converter
$V_{\alpha,PCC}$ $I_{\alpha,PCC}$	*AC* grid voltage and current in α coordinate measured at PCC, respectively
$V_{\alpha,ref}$ $I_{\alpha,ref}$	*AC* grid voltage and current references in α coordinate, respectively
$V_{\beta,PCC}$ $I_{\beta,PCC}$	*AC* grid voltage and current in β coordinate measured at PCC, respectively
$V_{\beta,ref}$ $I_{\beta,ref}$	*AC* grid voltage and current references in β coordinate, respectively
X/R	inductive-resistive characteristic
$x_{d,PCC}$, $x_{q,PCC}$	*AC* line state variables in d and q coordinates, respectively
x_{d1},x_{d2},x_{d3}, x_{q1},x_{q2},x_{q3}	PR state variables in d and q coordinates, respectively
x_v,x_q	outer controller state variables in d and q coordinates, respectively
ΔV_{DC}	DC voltage variation due to FSM function
ϑ	*AC* grid voltage angle
ω	*AC* grid nominal angular frequency and frequency parameter design for PR controller transfer fucntion
ω_{grid}	*AC* grid angular frequency

needed, as proposed in [11].

Based on the existing literature, *PR* controllers can be classified according to two main categories: the degree of similarity with ideal *PR* controller and the additional complementary feedback branches. According to the degree of similarity, in [15] three *PR* controller types are defined, namely, ideal, non-ideal and complex vector. As explained in [15], the complex vector *PR* controller presents the lowest sensitivity to integral gain and frequency variations around the fundamental frequency, in comparison to the ideal and non-ideal *PR* controllers. However, it is only stable if voltage decoupling is performed and its use is more adequate for applications such as droop controlled microgrids, where the resonant frequency changes. Nevertheless, [15] concludes that the presence of voltage decoupling branches is more important than the type of *PR* controller selected for inner control loop, since it greatly decreases the sensitivity of the *PR* controller to frequency variation.

According to the additional complementary feedback branches, [14,16] study *PR* controller configurations and compare them with the ideal *PR* controller configuration, where no complementary branches are included. The authors name these as *PRXF*, *PRXC* and *PRX2* controllers [14,16]. The outcomes of the comparison are summarized as follows. *PRXF* controller presents lower sensitivity than the ideal *PR* controller to frequency deviations around the resonant frequency in direct sequence but high in inverse sequence. *PRXC* controller presents lower sensitivity to frequency events around the resonant frequency than the ideal *PR* controller but higher that *PRXF* controller and it does not manage frequency events in inverse sequence. Eventually, *PRX2* controller is the configuration that mostly decreases the sensitivity to frequency deviations around resonant frequency both in direct and inverse sequences. Therefore, *PRX2* controller is most suited for those applications that require high robustness, such aerospace applications, due to the bigger frequency excursions (± 1Hz) that normally appear. In contrast, the frequency excursions which commonly happen in electrical networks are in the order of ± 50 mHz or ± 200 mHz at hour boundaries [17]. This fact makes ideal *PR*, *PRXF* or *PRXC* controllers more suitable for electrical grids and one of these three may be chosen depending on the characteristics of the power system under study. However, it is important to note that *PRXF* and *PRXC* controllers do not manage inverse sequence frequency excursions that may appear in the electrical power system. So, among these three *PR* configurations only ideal *PR* controller would give a reponse in inverse sequence.

With regard to power systems, their characteristics have an influence on the stability of the *VSC* current controller. Thus, it is of high importance to study the combined effect that changes on the *VSC* current controller parameters along with the *AC* grids parameters have on the stability of the system and of the *VSC* itself. An *AC* grid can be characterized by the Short Circuit Ratio (*SCR*) and the *X/R* ratio at the point of common coupling (*PCC*) of the *VSC*. *SCR* measures the *AC* grid strength while *X/R* ratio characterizes the inductive-resistive behaviour. In [18], a basic two-terminal single-pole *HVDC* transmission

system is analyzed taking into account variations of *AC* grid strength. They conclude that to withstand voltage fluctuation caused by *DC* commutation failure, the strength of the *AC* grid must be high enough to cope with this. In [19], the effect of grid impedance variation on the transient stability of an inverter is studied and results show that the *AC* line resistive component of these lines increases the asymptotic stability region of the system. The use of *SCR* and *X/R* ratio for stability analysis can be justified by considering the current *AC* grid context. On the one hand, the connection and disconnection events of generators and loads in the *AC* grid executed by grid operators and variations in the operation modes due to summer or winter peaks may change the short circuit capacity of the receiving end of an *AC* power system, especially in islanded grids [18]. Additionally, the variation of *X/R* ratio is also provoked by different operation modes of generators [20].

As it has been discussed in the previous paragraphs, many analysis regarding *PR* controller topologies and configurations with complementary branches have been object of study to see their frequency sensitiveness. Moreover, discrete implementations of *PR* controller are used, as in [21], to obtain a robust design of *PR* controller while dealing with digital implementation. There is yet a vast list of publications where the *PR* controller is modelled in continuous domain [11–16], their conclusions are proved against *EMT* models or, in some cases, against tests in laboratory setups. However, there has not been found a study where the influence on stability of *PR* controller parameters, in its ideal shape with voltage decoupling branches, is analysed when varying the *AC* grid configuration. Therefore, in this paper the effect of *PR* controller parameters on stability is studied for different *AC* grid configurations, parameterized through *SCR* and *X/R* ratio.

In [22], a similar methodology to the one used in this paper is employed, aimed at studying the stability of photovoltaic plants integrated in weak *AC* networks under the subsynchronous resonance phenomena: an analytical model is created (in that case by means of an impedance model rather than state-space equations), then developed model is validated against an *EMT* model, the stability analysis is carried out and the latter is finally verified by means of *EMT* simulations. The differences with the present paper are mainly, that *PI* controller is considered as inner current controller instead of *PR* controller, the type of generation case (specified only for photovoltaic plants while in the present case is not generation specific) and the phenomena under study, i.e. subsynchronous resonance phenomena in contrast to general instability issues.

In [23], the main authors of the present paper modelled a *PR* controller embedded in the control structure of a *VSC* terminal, which is part of an *HVDC* grid aimed at evacuating offshore wind power to onshore *AC* grids. The purpose of [23] was to validate a control scheme for the *HVDC* grid that also took into account the fulfilment of the UK Grid Code. Different fault tests were carried out in order to assess the system against different outages occurring at both *DC* and *AC* sides of the system, including frequency excursions and unbalanced 2-phase short circuits at the *PCC*. The response of the *PR* controller and the specific tuning of it, was proved to be successful under every outage that was tested.

Besides, in [24], the same *HVDC* grid as in [23] was used to validate the control architecture again, but in this time, against a specific model of an island with dynamic parameters which substitutes the *AC* grids considered in [23]. The dynamic model of the island included a synchronous generator controlled by a first order voltage control, governor and power setpoint generation blocks and several loads that were connected or disconnected depending upon the type of fault applied, i.e. voltage dips or frequency excursions. Different variations of dynamic inertia of the synchronous generator and length of the *AC* lines that compound the island model were applied under different frequency excursions and the stability of the system was ensured in all cases.

The focus of the present paper is to design a *PR* controller considering scenarios that encompass combined changes in *SCR* and *X/R* ratios due to eventualities of diverse nature in the *AC* grid, such as sudden opening or closing of a circuit breaker at a specific speed, new connections to distribution or transmission grids or the modification of distance between conductors in electrical lines, under others. The study sheds light on cases where the *PR* controller is well designed for a weak grid scenario, but loses stability with the change of the *X/R*.

The structure of this paper is as follows. In Section 2 the methodology followed in this paper is explained using a flowchart. The development of the small signal model is described in Section 3. In Section 4, the validation of the small signal model described in Section 3 is

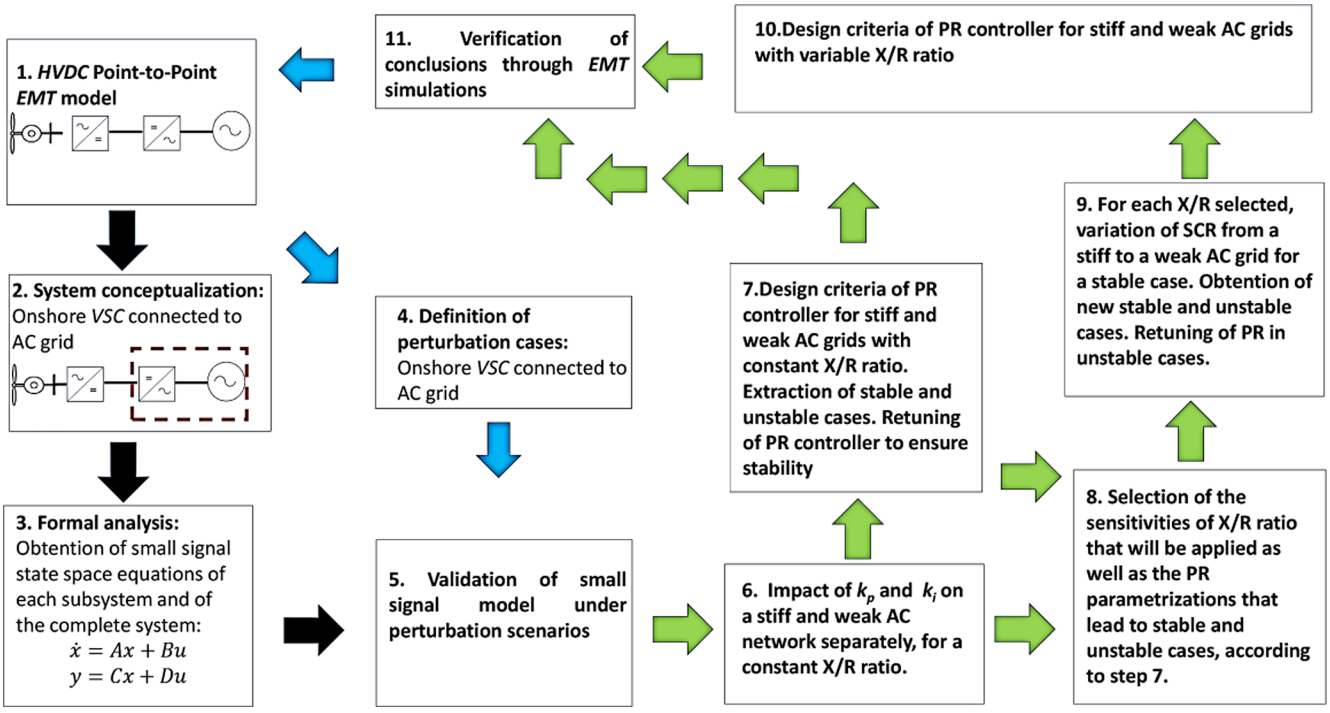

Fig. 1. Diagram of the methodology followed.

performed against *EMT* simulations. Section 5 details the eigenvalue trajectory analysis, thanks to which the proper tuning of PR controller is discussed under different scenarios that involve changes in *SCR and X/R ratios*. In Section 6, the previous modal analysis is verified in time domain with *EMT* simulations. Finally, conclusions are presented in Section 7.

2. Methodology

The methodology followed in this paper is represented in Fig. 1. It is composed by several stages. Initially (step 1 in Fig. 1), a baseline application consisting in a Point-to-Point *HVDC* link that conveys offshore wind energy to an onshore *AC* grid is considered and designated as the non-linear *EMT* reference model. The description of this model can be found in [23] and from here onwards, the interest of the present study is to develop a small signal analysis of the onshore *VSC* at the Point of Common Coupling (*PCC*), in connection several specific *AC* grid configurations. Although this is an application based analysis, the methodology described hereafter is suitable for any *VSC* converter connected to an *AC* grid. Considering this conceptualization (step 2 in Fig. 1), a small signal model of it is constructed by means of state-space equations defined by A,B,C and D matrixes (step 3 in Fig. 1). Proper linearizations are applied when necessary as will be shown in next sections. Afterwards, the small signal model is validated by using exported data from the *EMT* model. For this purpose, a large set of perturbation scenarios are simulated and the variables corresponding to the inputs(u) and ouputs(y) of the small signal model are exported from the *EMT* model (step 4 in Fig. 1). Then, the same perturbation scenarios are simulated in the small signal model and the small signal system response is verified through the exported data. Once the small signal model is validated for this large set of perturbation scenarios (step 5 in Fig. 1), the impact of *PR* parameters is evaluated separately in a stiff and weak *AC* grid with a constant *X/R* charateristic set to the benchmark value (step 6 in Fig. 1). This stage gives general design criteria for *PR* controller for stiff and weak *AC* grids (step 7 in Fig. 1) that have a constant *X/R* characteristic, and the retuning strategies for *PR* controller that ensures the system stability. Step 8 proposes a set of sensitivities upon which the *X/R* ratio can be varied by using the information provided by steps 6 and 7. Based on this, sensitivities of ± 10% and ± 20% in *X/R* ratio are studied in Section 5 for a *PR* parametrization corresponding to already stable case, according to the criteria extracted in step 6, for *AC* grids with a constant *X/R* characteristic. Step 9 aims at evaluating the impact of the *AC* grid strength whenever the selected sensitivities of *X/R* ratios are applied. In other words, step 9 evaluates the *PR* parameterization in terms of maintaining or losing stability whenever a different *X/R* ratio is considered. Based on the analysis conducted in step 9, general design criteria of PR controller for AC grids with variable X/R ratio is extracted and retuning strategies for *PR* controller are obtained. In step 11 the key analyzed cases and the two different design criteria for *PR* controller for constant and variable *X/R* characteristic are verified in the *EMT* model (step 10 in Fig. 1) to test the validity of the analysis.

3. VSC-AC small signal model

To assess the impact of *PR* controller parameters of a *VSC* and an *AC* grid configuration on the small signal stability of a *VSC-AC* system, the *VSC-AC* grid connection has been modelled in this section. The system configuration shown in Fig. 2 presents the *VSC-AC* grid connection system under study (enclosed in green rectangle) and the measurement and control system of the *VSC* converter.

The control schemes and technical data of the analysed *VSC-AC* grid connection, can be consulted in [23]. The small signal model of the system presented in Fig. 2, as it can be seen, consists of the outer and the inner controllers, composed by *PI* and *PR* controllers, respectively, as well as by an interface block that calculates the modulation indexes in αβ coordinates to be directly used as control inputs to the *VSC* converter. A more detailed descripcion of each control block, apart from the *VSC* and *AC* line models, is hereafter detailed. The state-space equations of each subsystem are derived and linearization stages, such as multiplications of inputs or coordinate transformation blocks, are carried out. Besides, the modelling approach of *PR* controller is discussed by taking into account the difference between the *AC* grid angular frequency (ω_{grid}) and the *PR* controller design frequency parameter (ω).

In the introduction section, a list of advantages and disadvantages of using dq or αβ frames have been indicated. Nevertheless, in the present paper the small signal model is implemented in dq reference due to two main reasons: on the one hand, the outer controller of the *VSC* converter is in dq coordinates and on the other hand, linear analysis is only

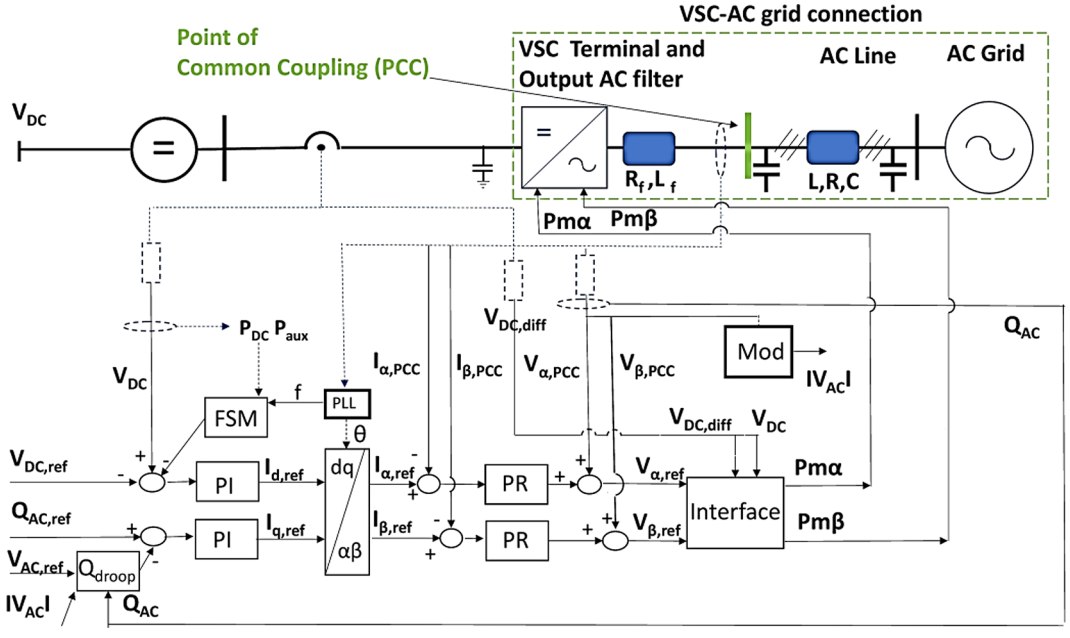

Fig. 2. System under study.

possible in dq frame, so the αβ frame is obviously discarded. With regard to the reference of dq coordinates, a synchronous reference frame is used with the d axis aligned to the a axis (abc frame).

Although the *AC* measurement filters at the *PCC* are implemented as first order delays in the *EMT* model, since harmonics are neither the focus of transient stability analysis nor the goal of the present paper, the *AC measurement* filters at the *PCC* can be safely discarded in the small signal model, as [25] proposes.

3.1. Outer controller

The outer controller is aimed at generating the dq current setpoints ($I_{d,ref}$ and $I_{q,ref}$) that enter the *PR* inner controller according to the *DC* voltage and reactive power control, respectively. The system is modelled in dq coordinates, so that active and reactive power can be controlled independently.

In the present case, the outer controller follows a Vdc-Q scheme [23] (Fig. 3), i.e. a scheme where *DC* voltage is controlled by means of the d current reference ($I_{d,ref}$) and where the reactive power is controlled by means of the q current reference ($I_{q,ref}$). Besides, the implemented outer control includes two discontinuous functions, named *FSM* and Qdroop , described below. However, with the purpose of having the model linearized around an specific operation point, these functions are considered to work only within their linear regions, in order to avoid non-linearities in the small signal model.

- The *FSM* function in this study is implemented to satisfy the *ENTSOE* regulation regarding overfrequency stability [26], and becomes active under overfrequency excursions for measurements greater than 50 Hz + deadband/2 and lower than 50.5 Hz. Its main objective is, whenever there is an overfrequency deviation, to calculate the DC voltage magnitude to be extracted (ΔV_{DC}) from the *DC* bus to restore the balance in the grid via a proportional constant (k_{FSM}) given by *ENSTOE*.

$$\Delta V_{DC} = k_{FSM} f + P_{DC,ref} - P_{aux} + FSM_{th} \tag{1}$$

where FSM_{th} corresponds to the y-intercept of a frequency dependent linear function and has been calculated to meet the limits of *FSM* mode dictated by *ENTSOE*. The *FSM* mode is active up to 50.5 Hz. When f exceeds 50.4 Hz the system also enters the *LFSM* mode [26], for which the DC power extracted from DC side is regulated according to the *ENTSOE* network code to meet primary frequency control standard.

- The Qdroop function, aimed at calculating reactive power variations based on *AC* voltage variations at the *PCC*, is also proposed by *ENTSOE* [27]. In (2) the computation of reactive power reference is modelled.

$$Q_{AC,ref} = k_{droop}(V_{AC} - V_{AC,ref}) \tag{2}$$

From the schemes presented in Fig. 3, state-space equations (3)–(6) are derived. Current dq references are obtained according to (5) and (6).

$$\dot{x_v} = -\frac{k_v}{T_v}V_{DC,ref} + \frac{k_v}{T_v}V_{DC} - \frac{k_v k_{FSM}}{T_v}f + \frac{k_v}{T_v}P_{DC,ref} - \frac{k_v}{T_v}P_{aux} + \frac{k_v}{T_v}FSM_{th} \tag{3}$$

$$\dot{x_q} = -\frac{k_{droop,AC}k_q}{T_q}V_{AC,ref} + \frac{k_{droop,AC}k_q}{T_q}V_{AC} \tag{4}$$

$$I_{d,ref} = x_v - k_v V_{DC,ref} + k_v V_{DC} - k_v k_{FSM} f + k_v P_{DC,ref} - k_v P_{aux} + k_v FSM_{th} \tag{5}$$

$$I_{q,ref} = x_q - k_{droop,AC}k_q V_{AC,ref} + k_{droop,AC}k_q V_{AC} \tag{6}$$

3.2. Inner PR controller

The inner *PR* controller implemented presents an ideal *PR* scheme and is responsible for generating the voltage references of the *VSC*, from the input of dq current references ($I_{d,ref}$ and $I_{q,ref}$) coming from outer controller, as shown in Fig. 4. Because of this and since the *PR* controller operates in αβ frame, there is a dq to αβ frame transformation block to accommodate the outer controller outputs, $I_{d,ref}$ and $I_{q,ref}$ in αβ coordinates. As the goal of this paper is to analyse small signal stability of the domain under study, a linear eigenvalues trajectory change is performed and this implies that the *PR* controller must be converted into dq coordinates. Therefore, two coordinate transformations (from dq to αβ and from αβ to dq) are required to obtain dq voltage references ($V_{d,ref}$ and $V_{q,ref}$). In between these two transformations, the main transfer function of ideal *PR* controller is found, which is dependent on angular frequency and designed upon the target angular frequency of interest.

In order to obtain the small signal model of this *PR* scheme, the inverse Park's transformation block from dq to αβ frame is equivalent to the addition $+j\omega_{grid} \approx j\omega$ to s terms in each transfer function shown in Fig. 4, as [11] explains. When achieved, the system presented in Fig. 4 becomes the one presented in Fig. 5.

In the present case, $\omega = 314.159$ rad/s is the angular frequency, based on which the *PR* transfer function is built, since this paper studies the influence of *PR* controller parameters on small signal stability at 50 Hz. However, the *AC* grid angular frequency (ω_{grid}) is not always equal to 314.159 rad/s, as it presents small fluctuations and this affects the linearization of the transformation due to the inclusion of this $+j\omega_{grid}$ term. Therefore, there are slightly small errors due to differences between ω and ω_{grid}, but considering previous papers that have worked with *PR* controllers in continuous domain [11–16], the $+j\omega_{grid} \approx j\omega$ approach is taken as valid.

Compared to Fig. 4, a different transfer function is found in Fig. 5, for which 3 state variables in each component (x_{d1}, x_{d2}, x_{d3} and x_{q1}, x_{q2}, x_{q3}, for d and q, respectively), are used. These are state variables derived from the process of linearization whose obtention is explained in detail in [11] and they correspond to the different polynomial degrees at the denominator of the transfer function observed in Fig. 5. The small signal equations resulting from the schemes presented in Fig. 5 are listed below.

$$\dot{x_{d1}} = x_{d2} \tag{7}$$

$$\dot{x_{d2}} = x_{d3} \tag{8}$$

$$\dot{x_{d3}} = -4\omega^2 x_{d2} - I_{d,PCC} + I_{d,ref} \tag{9}$$

$$\dot{x_{q1}} = x_{q2} \tag{10}$$

$$\dot{x_{q2}} = x_{q3} \tag{11}$$

$$\dot{x_{q3}} = -4\omega^2 x_{q2} - I_{q,PCC} + I_{q,ref} \tag{12}$$

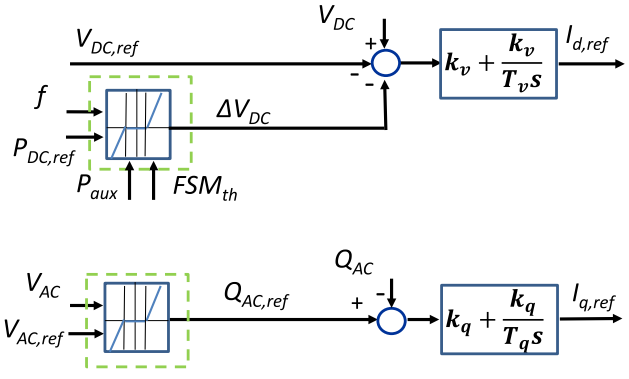

Fig. 3. Block diagram for Outer controller.

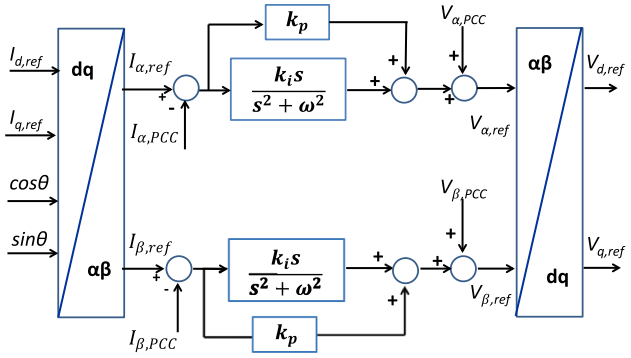

Fig. 4. *PR* scheme.

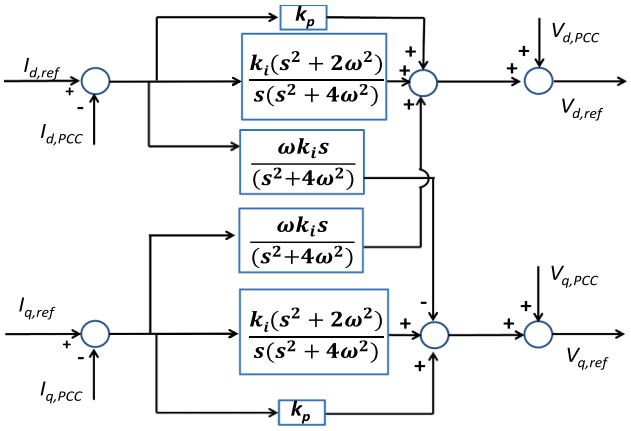

Fig. 5. Transformed *PR* scheme into dq coordinates.

$$V_{d,ref} = 2k_i\omega^2 x_{d1} + k_i x_{d3} + k_i\omega x_{q2} + V_{d,PCC} - k_p I_{d,PCC} + k_p I_{d,ref} \quad (13)$$

$$V_{q,ref} = 2k_i\omega x_{q1} + k_i x_{q3} - k_i\omega x_{d2} + V_{q,PCC} - k_p I_{q,PCC} + k_p I_{q,ref} \quad (14)$$

where (13) and (14) present the calculation of the *PR* controller outputs, i.e. the dq voltage references of the *VSC* converter.

3.3. Average converter model

The average converter model (Fig. 6(a)) is composed by the *VSC* and an interface block called "Normalization Block", whose aim is to calculate the modulation indexes of the *VSC* (*Pmd* and *Pmq*). The modulation indexes are obtained from the dq output voltage references of the *PR* controller and the measured *DC* voltage. In this particular case, the *VSC* is part of a bipolar *HVDC* system, so the voltage must be the average value of the positive and negative pole voltages (19)). Since the multiplication of variables is a non-linear operation, the linearization results into the sum of variables involved multiplied each of them by coefficients which turn to be the other variable in steady-state (sub-index "ss") regime, as Fig. 6(b) shows.

From the schemes presented in Fig. 6(b), (15)–(18) are derived, where (15) and (16) describe the behaviour of the normalization block and (17) and (18) describe the behaviour of the *VSC* converter.

$$Pmd = 0.7\frac{1}{V_{DC,diff,ss}}V_{d,ref} + 0.7V_{d,ref,ss}\frac{1}{V_{DC,diff}} \quad (15)$$

$$Pmq = 0.7\frac{1}{V_{DC,diff,ss}}V_{q,ref} + 0.7V_{q,ref,ss}\frac{1}{V_{DC,diff}} \quad (16)$$

$$V_{d,AC} = k_0 V_{DC,ss} Pmd + k_0 Pmd_{ss} V_{DC} \quad (17)$$

$$V_{q,AC} = k_0 V_{DC,ss} Pmq + k_0 Pmq_{ss} V_{DC} \quad (18)$$

$V_{DC,diff}$ is calculated according to (19), and it is the mean value of the positive and negative *DC* voltage measurents. It should be taken into account that Vdc- is negative.

$$V_{DC,diff} = \frac{V_{DC}^{+} - V_{DC}^{-}}{2} \quad (19)$$

3.4. VSC output filter and AC line model

The considered VSC output filter consists of resistive (R_f) and inductive (L_f) terms, according to the scheme presented in Fig. 7. The input voltages for this filter are the output VSC voltages, $V_{d,AC}$ and $V_{q,AC}$, calculated as indicated in (17) and (18). Apart from this, Fig. 7 details a π-Equivalent section of the *AC* line corresponding to a length equal to Δx, being Δx, a division of the total *AC* line length. The π-Equivalent model is built upon the *AC* line resistance (R), inductance (L) and parallel capacitance (C) per unit length.

For the sake of simplicity, only one π-Equivalent section is included in Fig. 7 and the corresponding equations are detailed in (20)–(27). On the one hand, the state variables corresponding to VSC output filter are i_{1d} and i_{1q} (20) and (21) and on the other hand, the remaining state variables correspond to the π-Equivalent section (22)–(27).

$$\dot{i_{1d}} = -\frac{R_f}{L_f}i_{1d} + \omega i_{1q} + \frac{1}{L}(V_{d,AC} - V_{1d}) \quad (20)$$

$$\dot{i_{1q}} = -\frac{R_f}{L_f}i_{1q} - \omega i_{1d} + \frac{1}{L}(V_{q,AC} - V_{1q}) \quad (21)$$

$$\dot{V_{1d}} = \frac{2}{C(\Delta x)}(i_{1d} - i_{2d}) + \omega V_{1q} \quad (22)$$

$$\dot{V_{1q}} = \frac{2}{C(\Delta x)}(i_{1q} - i_{2q}) - \omega V_{1d} \quad (23)$$

$$\dot{i_{2d}} = \frac{1}{L(\Delta x)}(V_{1d} - V_{2d} - R(\Delta x)i_{2d}) + \omega i_{2q} \quad (24)$$

$$\dot{i_{2q}} = \frac{1}{L(\Delta x)}(V_{1q} - V_{2q} - R(\Delta x)i_{2q}) - \omega i_{2d} \quad (25)$$

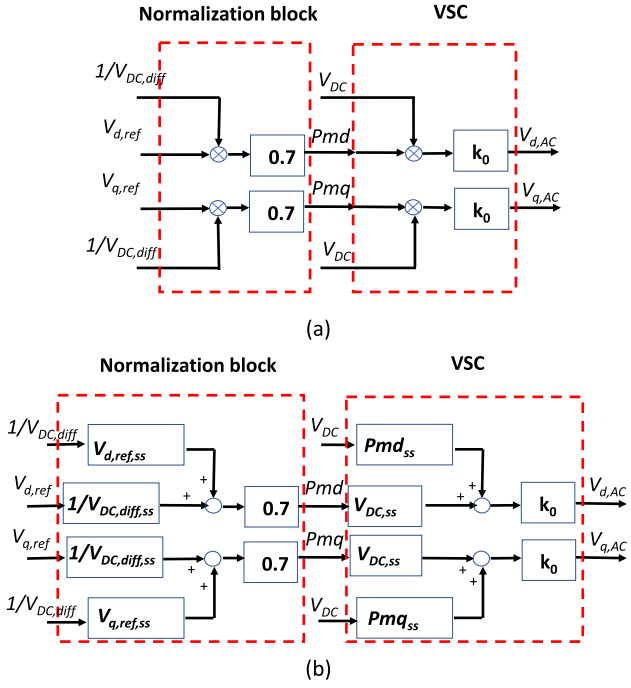

Fig. 6. (a) Normalization block and *VSC* converter in a non-linearized version and (b) Linearized Normalization block and *VSC* converter.

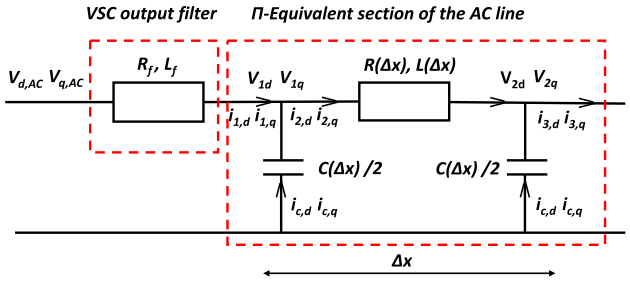

Fig. 7. *AC* line model.

$$\dot{V_{2d}} = \frac{2}{C(\Delta x)}(i_{2d} - i_{3d}) + \omega V_{2q} \tag{26}$$

$$\dot{V_{2q}} = \frac{2}{C(\Delta x)}(i_{2q} - i_{3q}) - \omega V_{2d} \tag{27}$$

Several π-Equivalent sections can be added in cascade to the one presented in Fig. 7, in order to improve the accuracy of the model in terms of frequency. The calculation of the number of π-Equivalent sections (N_{eq}) in order to meet a specific accuracy in terms of frequency, is detailed in (28) and (29) [28].

$$f_{max} = \frac{N_{eq}\upsilon}{8l} \tag{28}$$

$$\upsilon = \frac{1}{\sqrt{LC}} \tag{29}$$

Being f_{max} the required frequency response, ν the phase velocity, which depends on the capacitance(C) and inductance (L) of the *AC* line per unit of length, l the total length of the *AC* line and N_{eq} the minimum number of necessary π-Equivalent sections to achieve accuracy under the desired f_{max}. In the present paper, the N_{eq} number is considered to be 6, slightly greater than the minimum number of necessary π-Equivalent sections, considering the values for C and L given in Section 4.1.

The final outcomes of this subsystem composed by 6 π-Equivalent sections are the dq currents circulating through the *AC* line and the dq voltages at both ends of the *AC* line and at interface points between π-Equivalent sections.

3.5. Full small signal model

At this point, the small signal model equations of each subsystem that compound Fig. 2 have been presented along the section. The small signal model of the full system under study are described by (3)–(4), (5)–(6), (7)–(12), (20)–(27) and by also cascading the equations of five additional π-Equivalent sections, which present the same behaviour as described by (22)–(27).

The feedback branch connects the *AC* line model with the *PR* controller model, by making currents i_{1d} and i_{1q} and the voltages V_{1d} and V_{1q} of the *AC* line model, equal to $I_{d,PCC}$, $I_{q,PCC}$, $V_{d,PCC}$ and $V_{q,PCC}$, respectively, of the *PR* controller model.

The responses of the full small signal model with all variables substituted are shown in Annex I.

4. Small signal model validation against time domain simulations

In this section, the Base Case for *PR* parametrization is presented, justified and validated. The small signal model described in Section 3 has been implemented in Octave and the time domain simulations needed for its validation have been carried out in DIgSILENT PF software. The validation results of the small signal model are shown in this section through different perturbation scenarios. The selection of these values, namely $k_p = 1.5$ and $k_i = 5000$, is justified according to the results obtained in previous research carried out by the same main authors [23,24].

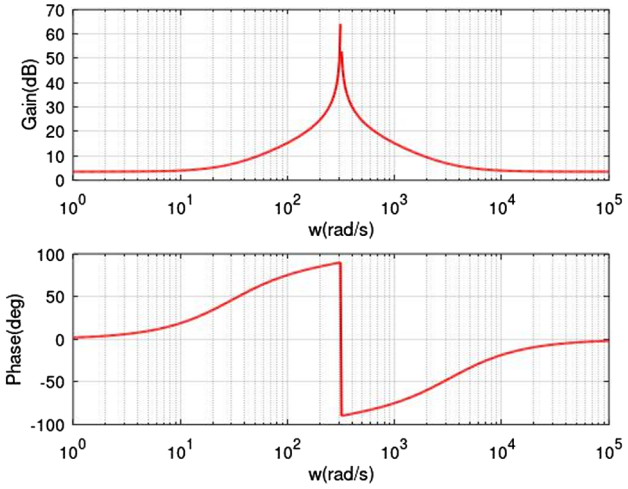

Fig. 8. Bode diagram of PR controller tuned at $k_p = 1.5$ and $k_i = 5000$.

Another reason is the provision of sufficient gain and phase margins, as far as the plant phase is limited between ± 90° at the frequencies affected by the resonant peak. Being the system described in Section 3 a Multiple Input-Multiple Output (MIMO) system, [29] holds that the phase and gain margins can be only used for Single Input-Single Output (SISO) systems to check system stability. Nevertheless, the bode diagram of the *PR* controller tuned at $k_p = 1.5$ and $k_i = 5000$, as a SISO system, has been obtained and is shown in Fig. 8. In Fig. 8, the gain and phase margins turn to be sufficient to ensure system small signal stability.

The rest of system parameters are defined in Table 1 and justified upon successful results in previous research in [23,24].

With the aim of validating the model described previously in Section 3, *EMT* simulations have been carried out. For this purpose, a set of scenarios have been defined to analyse the response under different perturbations. Basically, each scenario implies the perturbation of a set of input variables of the complete model presented in Fig. 2. These scenarios were designed and constructed to cover perturbations of all posible signals entering *VSC-AC* connection system. Due to space limitations, only results coming from the validation under specific scenarios are presented, where a perturbation of 5% of the reference value has been applied to both $V_{DC,ref}$ and $V_{AC,ref}$ inputs of the system, as shown in Fig. 8(a) and (b) respectively, and a perturbation of 0.3% change in *AC* grid frequency (Fig. 9 (c))is applied to enter in the *FSM* range[26].

Table 1
Network and VSC parameters.

Rated *DC* Voltage (kV)	640
Rated *AC* Voltage (kV)	275
Rated *VSC* power (MVA)	560
VSC output filter-R_f (p.u)	0.01
VSC output filter-L_f (p.u)	0.035
AC line series resistance (Ohm/km)	0.015
AC line series inductance (mH/km)	0.4
AC line parallel capacitance (μF/km)	0.22
AC line X/R ratio	8.37
AC line length (km)	1
ω-Resonant angular frequency-Proportional Resonant control (rad/s)	314.159
Proportional Constant-Reactive Power Control (k_q)	0.4 pu
Time Constant-Reactive Power Control (T_q)	0.01 s
Filter Time Constant-*DC* Voltage (T_{rVDC})	0.01 s
Filter Time Constant -Reactive Power (T_{rq})	0.02 s
Dead-band droop *AC* Voltage	0.005 pu
AC Voltage set-point ($V_{AC,ref}$)	1pu
Proportional Constant-*DC* Voltage Control (k_v)	15 pu
Time Constant-*DC* Voltage Control (T_v)	0.05 s

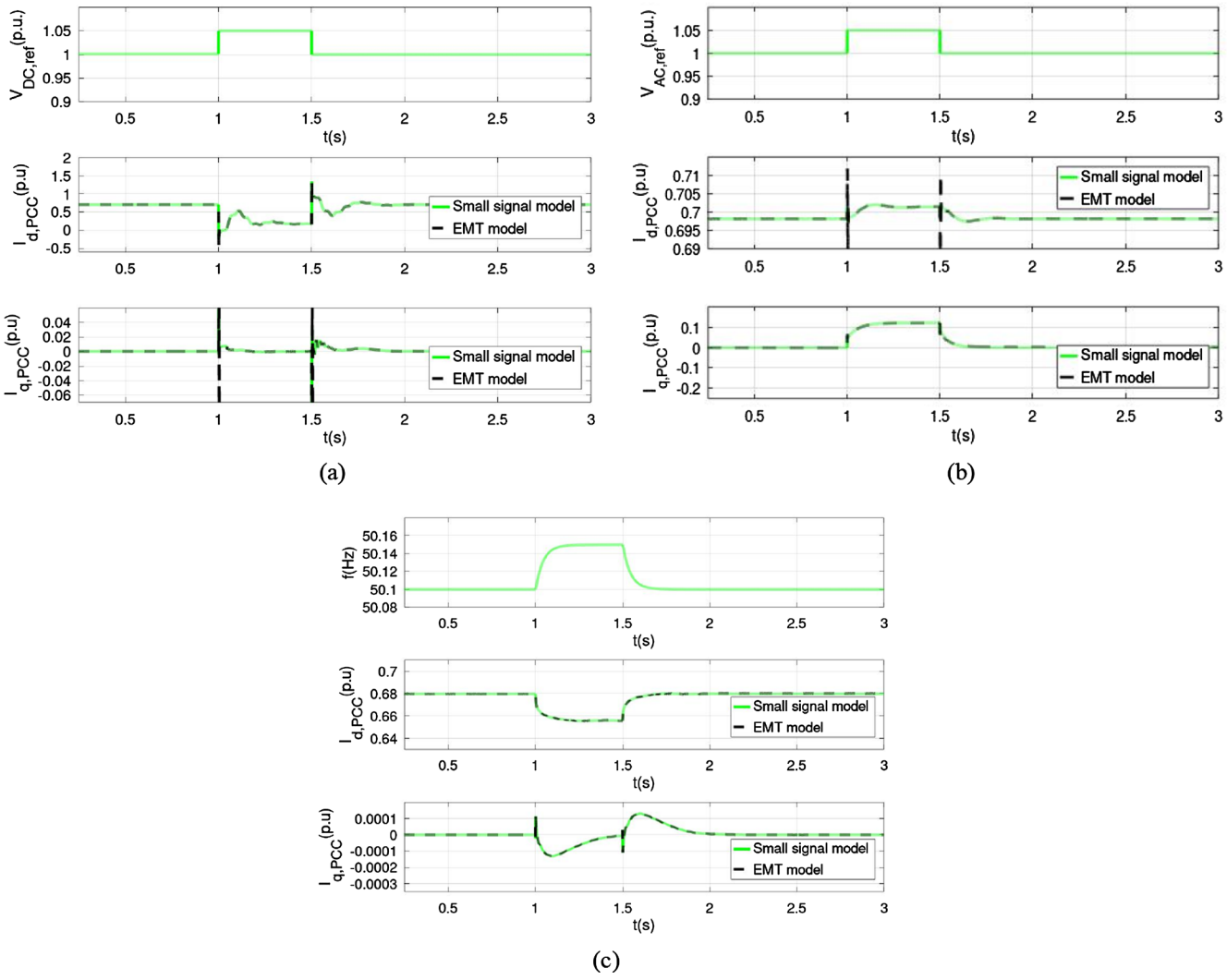

Fig. 9. Comparison of responses in small signal model (green) and in *EMT* model (discontinuous black) under different perturbation scenarios: (a) 5% of change of $V_{DC,ref}$, (b) 5% of change of $V_{AC,ref}$ and (c) 0.3% change of f. (For interpretation of the references to colour in this figure legend, the reader is referred to the web version of this article.)

In Fig. 9, the outputs coming from the small signal model match the responses from the *EMT* model under the different perturbation scenarios shown, which cover changes in $V_{DC,ref}$, $V_{AC,ref}$ and f. There is a small degree of uncertainty between the responses of the *EMT* and the small signal models, which corresponds to the precision of the algorithms. Nevertheless, the validation ensures that the small signal model captures small signal variations around different linearization points of the *EMT* model. This can also be observed in the literature [9,30].

It can be concluded that deviations in $V_{DC,ref}$ input, have a larger influence of the d current component ($I_{d,PCC}$) and those in $V_{AC,\ ref}$ affect q current component ($I_{q,PCC}$) more. However, changes in $V_{DC,ref}$ are more critical than those in $V_{AC,ref}$ since a large change in the outputs (from 0.65 p.u. to 0 p.u in $I_{d,PCC}$) is observed in perturbation scenario (a) than in scenario (b) (from 0 p.u to 0.1 p.u. in $I_{q,PCC}$). Besides, minor excursions in *AC* grid frequency result into a smaller influence in both d and q responses.

5. Eigenvalue trajectory analysis

In this section two small signal analysis are considered, in order to account, on the one hand, for the variable nature of *AC* grid strength and, on the other hand, for the fluctuating character of X/R characteristic in a context of an *AC* grid with dynamic events. Therefore, the analysis is divided in two stages.

- Firstly, the impact of PR controller parameters on the small signal stability is evaluated separately in a stiff and in a weak *AC* grid where the X/R characteristics remains constant and equal to the benchmark value.
- Secondly, the impact of PR controller parameters on the small signal stability is evaluated for a changing X/R characteristic.

Modifications in *X/R* ratio imply changes in the current angle but not in the line impedance. Therefore, changes in *X/R* ratio may not depend directly on *SCR* variations. However, since SCR varies more often than X/R feature, the analysis for different X/R values is carried out also considering the variability of SCR.

The changes in *SCR* in the *EMT* model are performed by varying the length of the *AC* line that connects the *AC* grid with the *VSC* converter. Several short circuits are calculated in the *EMT* model to see which length must have the *AC* grid line to account for two specific *SCR* measured at the *PCC*, according to a weak *AC* grid (*SCR* = 1) and a stiff *AC* grid (*SCR* = 25). The value for stiff *SCR* has been selected according to [31,32]. Afterwards, the two length values of the *AC* line which lead to a weak and a stiff *AC* grid at the *PCC* are noted. When performing the analysis in the small signal model, in order to have different *SCR* values,

the length of the *AC* line is modified between these two extreme length values. Therefore, the variation of the *AC* line length value is equivalent to the variation of the corresponding *SCR* value. While doing this change, the *X/R* ratio is constant as being *X/R* independent from the *AC* line length.

5.1. Impact of PR controller parameters in AC grids with variable strength for a constant X/R characteristic

The analysis begins with an evaluation of how the variation of *PR* controller parameters, i.e. k_p and k_i, affect the stability of the system whenever a stiff or a weak *AC* grid is considered. This stage is intended for scenarios which consider a constant X/R characteristic equal to the benchmark value, i.e 8.37. In Fig. 10, this analysis is achieved for a stiff *AC* grid ($SCR = 25$) by varying k_p (Fig. 10(a)) and k_i (Fig. 10(b)).

It can be seen that the system is stable for every trajectory derived in k_p and k_i. However, the reduction of k_p diminishes the stability margin as it pushes the eigenvalues towards the imaginary axis. As for the effect of k_i, its increment also causes trajectories in the right direction while it increases the oscillatory component of the eigenvalues with greater absolute real component.

As for the case of a weak *AC* grid ($SCR = 2.73$), the trajectories of eigenvalues derived from changes in k_p and k_i are presented in Fig. 11(a) and (b), respectively.

It can be seen in Fig. 11 that as far as k_p decreases, the eigenvalues closer to the imaginary axis and for values lower that 1 drive the system to the unstable area.

In Fig. 11(b), k_i has been varied from 5000 to 20,000 and the trajectory initially shows the eigenvalues getting closer to the imaginary axis but then moving away from it and increasing both the oscillatory and the real component. Nevertheless, the trajectory derived from the change in k_i keeps the system between the stability boundaries.

5.2. Impact of PR controller parameters in AC grids with variable strength for a variable X/R characteristic

The *X/R* characteristic of an *AC* grid can change as a function of the localization, type and length of *AC* lines, the voltage at which they are connected, under others. Even in the case that X/R ratio does not change, VSC converters must be designed to work properly when subjected to variations in one or more characteristics previously mentioned.

In order to have a complete view of the fluctuating effect of X/R ratio in an *AC* grid with variable strength, a sensitivity analysis of X/R ratio variations is suggested, taking the benchmark X/R value used in Section 5.1, i.e. $X/R = 8.37$, as the reference upon which the modifications are achieved. The developed methodology in this paper proposes for unstable cases the modification of *PR* controller parameters in order to return the system to stability again.

According to the analysis conducted in Section 5.1, $k_p = 1.07$ and $k_i = 5000$ have been selected as a *PR* controller parameterization which ensures stability in both stiff and weak *AC* networks, whenever the *X/R* ratio is kept constant to the benchmark value, i.e. $X/R = 8.37$.

Therefore, the system with the mentioned *PR* parameterization is subjected to a ± 10% change in X/R value and the trajectories of eigenvalues are shown in Fig. 12(a) and (b) for $X/R = 7.5$ and $X/R = 9.2$, respectively. It is also subjected to ± 20% variations, i.e. $X/R = 6.61$ and $X/R = 10$, which are shown in Fig. 12(c) and (d), respectively.

It can be seen in Fig. 12 that, although the change in X/R ratio in general move the eigenvalues closer to the imaginary axis, at ± 10% and + 20% *X/R* variations the stability of the system is kept. However, at the −20% *X/R* variation the eigenvalues cross the imaginary axis and drive the system to instability. This trajectory demonstrates that, although the PR controller was well designed for a stiff and weak *AC* grid configuration, a −20% variation of X/R in a weak AC grid makes the system move out from the stable region.

For the unstable case shown in Fig. 12(c), two proposals of change in *PR* controller parameters are presented, one based in the retuning of k_p (Fig. 13(a)), and the other on the retuning of k_i(Fig. 13(b)).

In general, changes in k_p or k_i over 10% of their initial values are required to return the system to stability. However, since the increase of k_i implies the rise of the oscillatory component, changes in k_p are preferable since they maintain the frequency of the closest eigevalues to the imaginary axis. Two stable cases for $X/R = 6.61$ presented in Fig. 13(a) and (b) have been chosen to be verified against EMT simulations.

6. Verification of small signal analysis against *EMT* simulations

Simulations in DIgSILENT PowerFactory software have been performed to verify the previous modal analysis in *EMT* time domain. The main reason for this verification is the fact that eigenvalue trajectory analysis is a linear tool, while EMT simulations consider non-linearities that give a better approach to reality.

In this section several key scenarios extracted in Section 5 are verified for an integration step size of 1 μs. For this purpose, the same perturbation in VDC,ref of Fig. 9(a) is applied to verify the previous analysis. The response of the output variables for different PR parametrizations, SCR and X/R values is observed. Results in red show values corresponding to left vertical axis and results in green show those corresponding to right vertical axis.

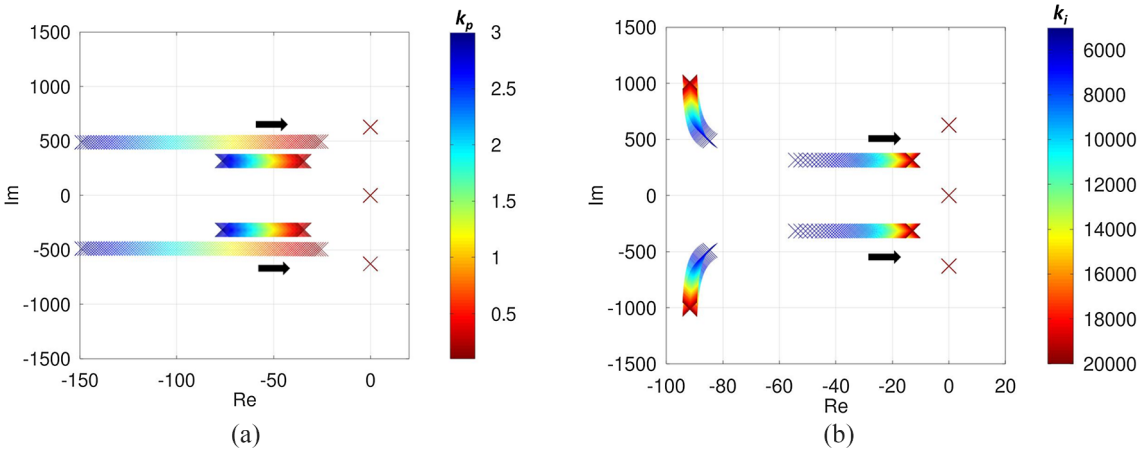

Fig. 10. Trajectory of eigenvalues in a stiff *AC* grid when *PR* controller parameters are varied: (a) k_p between 3 and 0.1 while $k_i = 5000$ and (b) k_i between 5000 and 20,000 while $k_p = 1.5$.

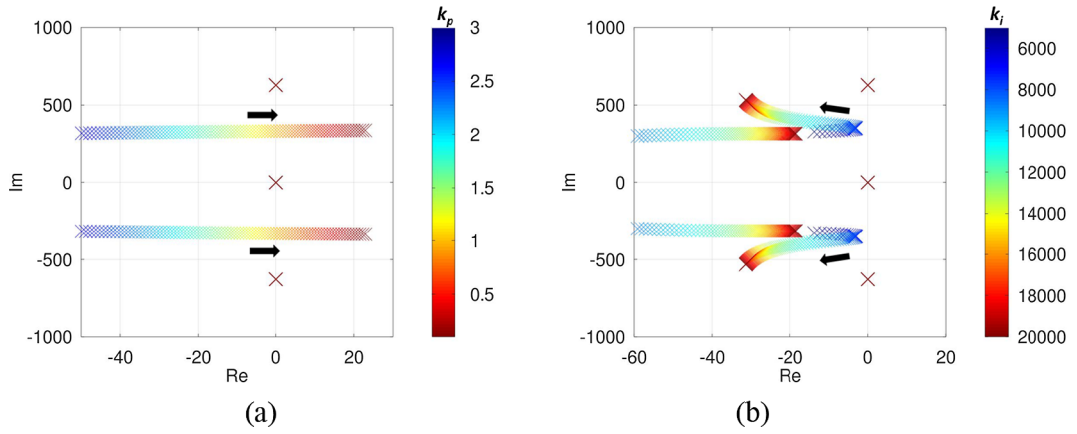

Fig. 11. Trajectory of eigenvalues in a weak *AC* grid when *PR* controller parameters are varied: (a) k_p between 3 and 0.1 while $k_i = 5000$ and (b) k_i between 5000 and 20,000 while $k_p = 1.5$.

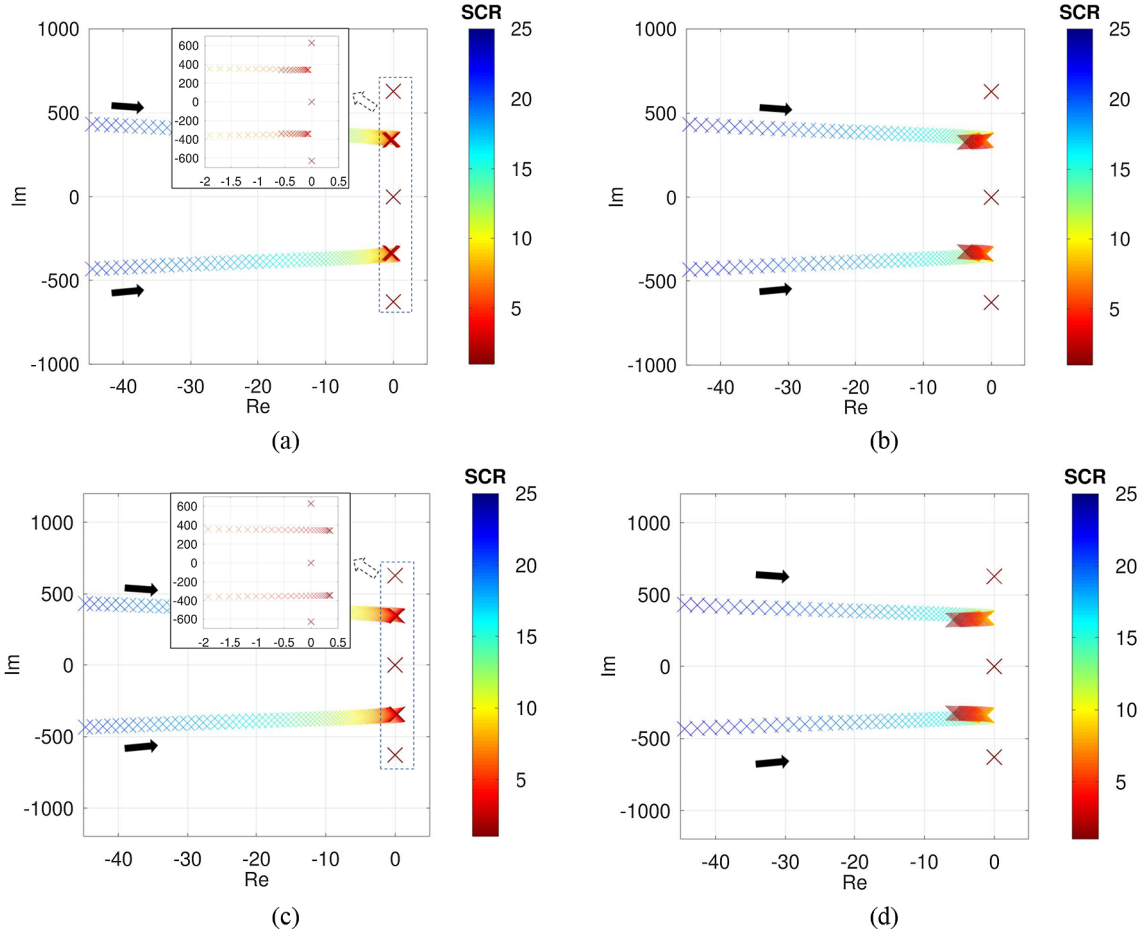

Fig. 12. Trajectory of eigenvalues for SCR ratio change:25 → 1 with $k_p = 1.07$ and $k_i = 5000$ for different levels of X/R change: (a)-10% (X/R = 7.5), (b) 10% (X/R = 9.2), (c) −20% (X/R = 6.61) and (d) 20% (X/R = 10).

In Fig. 14 two cases of weak *AC* grids under the same *PR* controller parameter tuning which differ in the *X/R* ratio are presented. The simulations show how a combination of *PR* controller parameters that ensured stability for the benchmark *X/R* ratio is lost when a −20% change in *X/R* magnitude is applied.

The signal shown in Fig. 14 corresponding to X/R = 6.61 loses the stability after the perturbation is cleared, which evidences that the *PR* controller parameters are inadequate for this specific weak *AC* grid case and points out to the need of retuning of *PR* controller. This retuning is shown in a form of two solutions presented in Fig. 15, where the blue signal is the "Solution 1", which is based on the change of k_p while k_i value is kept, and where the pink signal is the Solution 2", which corresponds to a proposal of changing k_i while k_p is kept.

The signals presented in Fig. 15 recover to the level prior to the perturbation, which allow the control system to operate the *VSC* jointly with the *AC* grid without risk of instability. Therefore, the small signal model jointly with the eigenvalue trajectory analysis developed in Section 5 have been verified, since the EMT simulations give similar results.

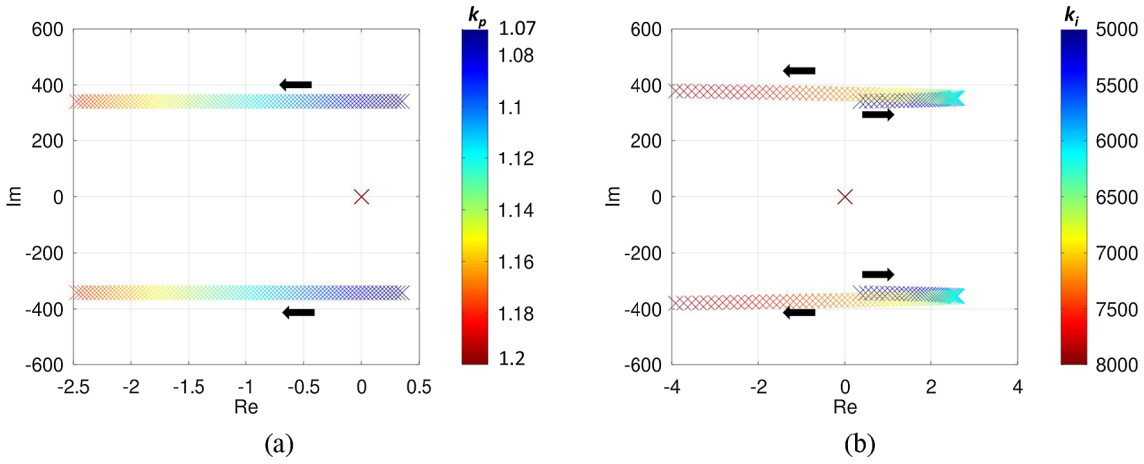

Fig. 13. Proposal of *PR* controller parameters' change to return the system to stability at a −20% deviation of X/R ratio and SCR = 1. (a) Change of $k_p = 1.07 \rightarrow 1.2$ with a fixed $k_i = 5000$, (b) Change of $k_i = 5000 \rightarrow 8000$ with a fixed $k_p = 1.07$.

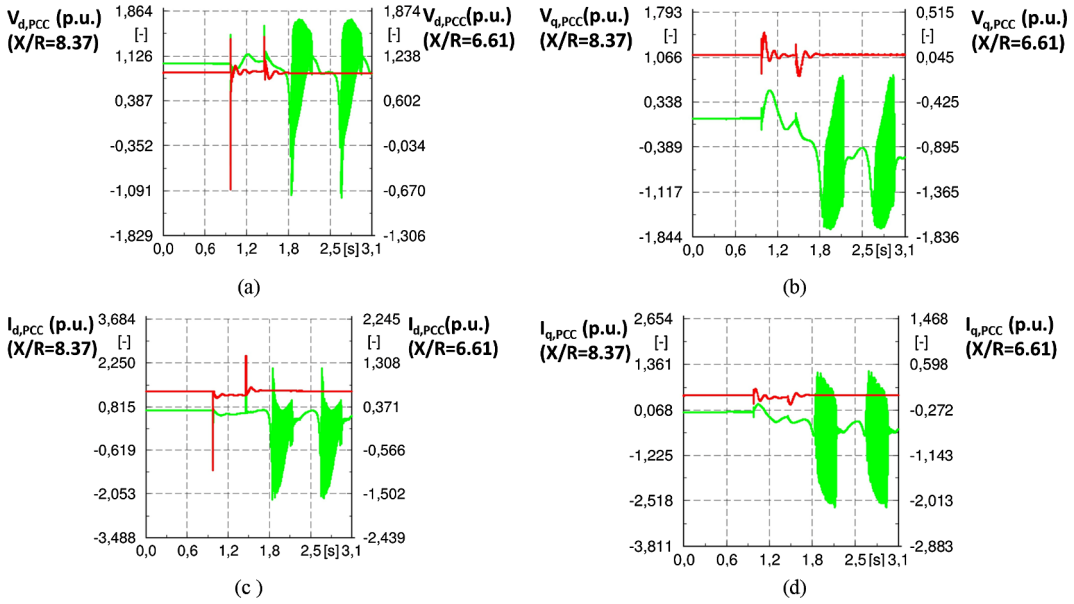

Fig. 14. Verification of stability for *AC* weak grid cases with PR controller tuned at $k_p = 1.07$ and $k_i = 5000$ with different X/R values: X/R = 8.37 (red) and X/R = 6.61 (green) under under a perturbation in $V_{DC,ref}$: (a) $V_{d,PCC}$, (b) $V_{q,PCC}$, (c) $I_{d,PCC}$ and (d) $I_{q,PCC}$. (For interpretation of the references to colour in this figure legend, the reader is referred to the web version of this article.)

7. Conclusions

In this paper a methodology for the definition of scenarios made upon combined changes in *SCR* and *X/R* ratios for *PR* controller design in *VSCs* has been proposed. This methodology has shed light on cases, where the *PR* controller is well designed for a weak grid scenario, but loses stability with the change of the *X/R*. Several conclusions can be extracted from this paper.

The analysis conducted concludes with different *PR* controller design criteria for weak and stiff *AC* grids. According to the stiff nature of an *AC* grid, the *PR* controller can be designed by considering the following criteria.

- In strong *AC* grids, k_p and k_i can take generally any value without losing stability, according to the trajectories derived. However, as far as k_p is reduced or k_i increased, the stability margin is reduced as it implies movements of eigenvalues in the right direction.
- In weak *AC* grids, low values of k_p can drive the system to instability while the general effect of increasing k_i is to enhance stability by moving the eigenvalues to the left side. In weak *AC* grids, the tradeoff of increasing k_i is the rise of oscillatory component of eigenvalues with greater absolute real component.

The analysis also concludes with different *PR* controller design criteria for weak *AC* grids whenever they present a X/R ratio deviated from the benchmark value.

- The eigenvalue trajectory analysis shows that, although the PR controller was well designed for a stiff and weak AC grid configuration, a −20% variation of X/R makes the system move out from the stable region. In general, changes in k_p or k_i over the 10% of their previous values are required to return the system to stability. However, since the increase of k_i implies the rise of the oscillatory component, changes in k_p are preferable since they maintain the frequency of the closest eigevalues to the imaginary axis.

Finally, the key cases derived from small signal analysis are verified against EMT simulations which reproduce perturbations in the DC voltage set-point. Within this verification, the stable cases show that signals recover to the level prior to the perturbation in contrast to

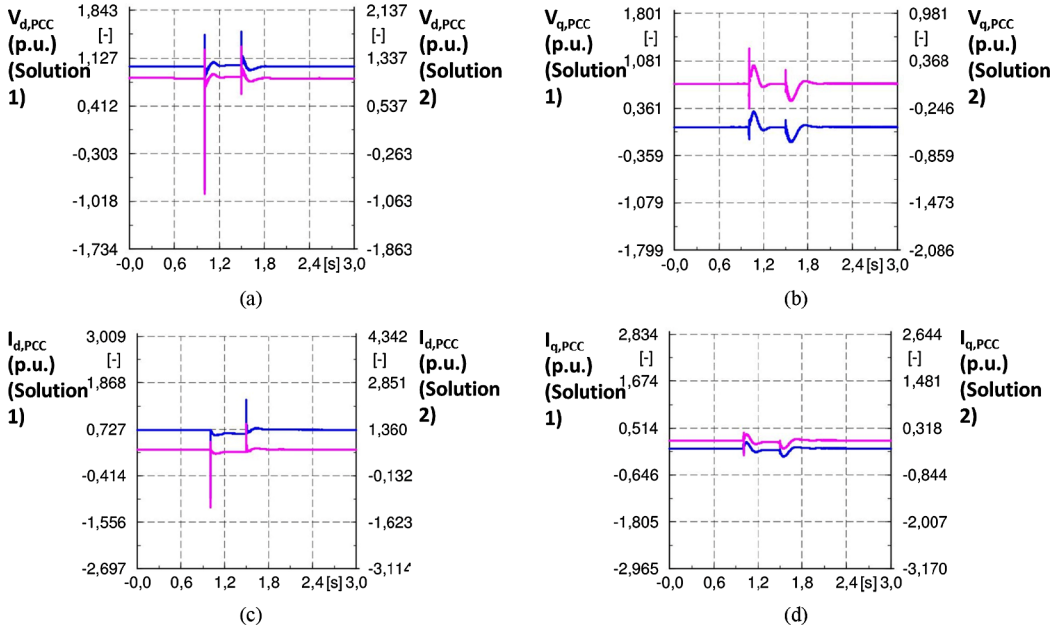

Fig. 15. Verification of solutions that return the system to stability for X/R = 6.61 in Fig. 13(a) (blue) and in Fig. 13(b) (pink) under a perturbation in $V_{DC,ref}$: (a) $V_{d,AC}$, (b) $V_{q,AC}$, (c) $I_{d,PCC}$ and (d) $I_{q,PCC}$. (For interpretation of the references to colour in this figure legend, the reader is referred to the web version of this article.)

unstable cases, where the signal loses the stability after the perturbation is cleared. This evidences that the PR controller parameters are inadequate for several specific weak AC grid cases with varying X/R ratio and points out to the need of retuning the PR controller. Two retuning strategies of PR controller have also been validated, as they present stable signals. Therefore, the conclusions obtained in linear eigenvalue trajectory analysis are validated by means of this verification procedure, since the EMT simulations give similar results.

In the end, the whole research study can be viewed as a resonance problem between VSC, PR controller parameters, *AC* grid strength and inductive-resistive characteristic. The capacity of evacuating power under stable conditions is compromised by *PR* parametrization, by the *AC* grid strenght and its inductive-resistive characteristic.

Acknowledgements

The authors thank the support from the Basque Government (projects: ELKARTEK KK-2017/00083 and Road2DC. KK-2018/00083 and research group GISEL ref. IT1083-16) and from the Ministry of Economy, Industry and Competitiveness (project ENE2016-79145-R AEFI/FEDER, UE).

Annex I

Small signal equations corresponding to the responses of the system with substituted variables.

Small signal responses of Inner *PR* controller:

$$V_{d,ref} = 2k_i\omega^2 x_{d1} + k_i x_{d3} + k_i\omega x_{q2} + V_{d,PCC} - k_p I_{d,PCC} + k_p x_v - k_p k_v V_{DC,ref} + k_p k_v V_{DC} - k_p k_v k_{FSM} f + k_p k_v P_{DC,ref} - k_p k_v P_{aux} + k_p k_v FSM_{th}$$

$$V_{q,ref} = 2k_i\omega x_{q1} + k_i x_{q3} - k_i\omega x_{d2} + V_{q,PCC} - k_p I_{q,PCC} + k_p x_q - k_p k_q k_{droop,AC} V_{AC,ref} + k_p k_q k_{droop,AC} V_{AC}$$

Small signal responses of Average Converter Model:

$$Pmd = 2k_i\omega^2 0.7V_{DC,diff,ss} x_{d1} + 0.7V_{DC,diff,ss} k_i x_{d3} + k_{diff} k_i\omega x_{q2} + 0.7V_{DC,diff,ss} V_{d,PCC} - 0.7V_{DC,diff,ss} k_p I_{d,PCC} + 0.7V_{DC,diff,ss} k_p x_v - 0.7V_{DC,diff,ss} k_p k_v V_{DC,ref} + 0.7V_{DC,diff,ss} k_p k_v V_{DC} - 0.7V_{DC,diff,ss} k_p k_v k_{FSM} f + 0.7V_{DC,diff,ss} k_p k_v P_{DC,ref} - 0.7V_{DC,diff,ss} k_p k_v P_{aux} + 0.7V_{DC,diff,ss} k_p k_v FSM_{th} + 0.7V_{d,ss} V_{DC,diff}$$

$$Pmq = 2k_i\omega^2 0.7V_{DC,diff,ss} x_{q1} - 0.7V_{DC,diff,ss} k_i\omega x_{d2} + 0.7V_{DC,diff,ss} k_i x_{q3} + 0.7V_{DC,diff,ss} V_{q,PCC} - 0.7V_{DC,diff,ss} k_p I_{q,PCC} + 0.7V_{DC,diff,ss} k_p x_q - 0.7V_{DC,diff,ss} k_p k_q k_{droop,AC} V_{AC,ref} + 0.7V_{DC,diff,ss} k_p k_q k_{droop,AC} V_{AC} + 0.7V_{q,ss} V_{DC,diff}$$

$$V_{d,AC} = 2\omega^2 k_0 V_{DC,ss} 0.7V_{DC,diff,ss} k_i x_{d1} + k_0 V_{DC,ss} 0.7V_{DC,diff,ss} k_i x_{d3} + k_0 0.7V_{DC,diff,ss} k_{diff} k_i\omega x_{q2} + k_0 V_{DC,ss} 0.7V_{DC,diff,ss} V_{d,PCC} - k_0 V_{DC,ss} 0.7V_{DC,diff,ss} k_p I_{d,PCC} + k_0 V_{DC,ss} 0.7V_{DC,diff,ss} k_p x_v - k_0 V_{DC,ss} 0.7V_{DC,diff,ss} k_p k_v V_{DC,ref} + (k_0 V_{DC,ss} 0.7V_{DC,diff,ss} k_p k_v + k_0 Pmd_{ss}) V_{DC} - k_0 V_{DC,ss} 0.7V_{DC,diff,ss} k_p k_v k_{FSM} f + k_0 V_{DC,ss} 0.7V_{DC,diff,ss} k_p k_v P_{DC,ref} - k_0 V_{DC,ss} 0.7V_{DC,diff,ss} k_p k_v P_{aux} + k_0 V_{DC,ss} 0.7V_{DC,diff,ss} k_p k_v FSM_{th} + 0.7k_0 V_{DC,ss} V_{d,ref,ss} V_{DC,diff}$$

$$V_{q,AC} = 2\omega^2 k_0 V_{DC,ss} 0.7V_{DC,diff,ss} k_i x_{q1} + k_0 V_{DC,ss} 0.7V_{DC,diff,ss} k_i x_{q3} - k_0 V_{DC,ss} 0.7V_{DC,diff,ss} k_i\omega x_{d2} + k_0 V_{DC,ss} 0.7V_{DC,diff,ss} V_{q,PCC} - k_0 V_{DC,ss} 0.7V_{DC,diff,ss} k_p I_{d,PCC} + k_0 V_{DC,ss} 0.7V_{DC,diff,ss} k_p x_q - k_0 V_{DC,ss} 0.7V_{DC,diff,ss} k_p k_q k_{droop,AC} V_{AC,ref} + k_0 V_{DC,ss} 0.7V_{DC,diff,ss} k_p k_q V_{AC} + 0.7k_0 V_{DC,ss} V_{q,ref,ss} V_{DC,diff} + k_0 Pmq_{ss} V_{DC}$$

References

[1] Khazaei J, Idowu P, Asrari A, Shafaye AB, Piyasinghe L. Review of HVDC control in weak *AC* grids. Electr Power Syst Res 2018;162:194–206. https://doi.org/10.1016/j.epsr.2018.05.022.

[2] Jovcic D, Lamont L, Abbott K. Control system design for VSC transmission. Electr Power Syst Res 2007;77:721–9. https://doi.org/10.1016/j.epsr.2006.06.011.

[3] Sanchez S, Bergna G, Tedeschi E. Tuning of control loops for grid-connected modular multilevel converters under a simplified port representation for large system studies. Twelfth international conference on ecological vehicles and renewable energies (EVER) 2017;2017:1–8. https://doi.org/10.1109/EVER.2017.7935913.

[4] Li Y, Yang S, Wang K, Zeng D. Research on PI controller tuning for VSC-HVDC system. 2011 International conference on advanced power system automation and protection 2011. p. 261–4. https://doi.org/10.1109/APAP.2011.6180414.

[5] Freytes J, Papangelis L, Saad H, Rault P, Cutsem TV, Guillaud X. On the modeling of MMC for use in large scale dynamic simulations. 2016 Power systems computation conference (PSCC) 2016. p. 1–7. https://doi.org/10.1109/PSCC.2016.7540938.

[6] Pinares G. Analysis of the DC dynamics of VSC-HVDC systems connected to weak AC grids using a frequency domain approach. 2014 Power systems computation conference 2014. p. 1–7. https://doi.org/10.1109/PSCC.2014.7038406.

[7] Amin M, Molinas M. Small-signal stability assessment of power electronics based power systems: a discussion of impedance- and eigenvalue-based methods. IEEE Trans Ind Appl 2017;53:5014–30. https://doi.org/10.1109/TIA.2017.2712692.

[8] Amin M, Suul JA, D'Arco S, Tedeschi E, Molinas M. Impact of state-space modelling fidelity on the small-signal dynamics of VSC-HVDC systems. 11th IET international conference on AC and DC power transmission 2015. p. 1–11. https://doi.org/10.1049/cp.2015.0048.

[9] Saad H, Mahseredjian J, Dennetière S, Nguefeu S. Interactions studies of HVDC–MMC link embedded in an *AC* grid. Electr Power Syst Res 2016;138:202–9. https://doi.org/10.1016/j.epsr.2016.02.029.

[10] Kotb O, Ghandhari M, Eriksson R, Sood VK. On small signal stability of an *AC*/DC power system with a hybrid MTDC network. Electr Power Syst Res 2016;136:79–88. https://doi.org/10.1016/j.epsr.2016.02.004.

[11] Lehn PW, Podrucky S. Small-signal modeling of power electronic converters with resonant controllers. International conference on power systems transients (IPST2009), Kyoto, Japan. 2009. p. 6 http://ipstconf.org/papers/Proc_IPST2009/09IPST063.pdf.

[12] Teodorescu R, Blaabjerg F, Liserre M, Loh PC. Proportional-resonant controllers and filters for grid-connected voltage-source converters. IEE Proc – Electr Power Appl 2006;153:750. https://doi.org/10.1049/ip-epa:20060008.

[13] Zhang N, Tang H, Yao C. A systematic method for designing a PR controller and active damping of the LCL filter for single-phase grid-connected PV inverters. Energies 2014;7:3934–54. https://doi.org/10.3390/en7063934.

[14] Hwang JG, Lehn PW, Winkelnkemper M. A Generalized class of stationary frame-current controllers for grid-connected *AC*–DC converters. IEEE Trans Power Delivery 2010;25:2742–51. https://doi.org/10.1109/TPWRD.2010.2045136.

[15] de Bosio F, Pastorelli M, Ribeiro LAdS, Lima MS, Freijedo F, Guerrero JM. Current control loop design and analysis based on resonant regulators for microgrid applications. IECON 2015 – 41st annual conference of the IEEE industrial electronics society 2015. p. 005322–7. https://doi.org/10.1109/IECON.2015.7392938.

[16] Ngo T, Santoso S. Improving proportional-resonant controller for unbalanced voltage and frequency variation grid. 2016 IEEE/PES transmission and distribution conference and exposition (T D) 2016. p. 1–5. https://doi.org/10.1109/TDC.2016.7520071.

[17] UCTE AD-HOC Group, Frequency quality investigation. Excerpt of final report; n.d. https://www.entsoe.eu/fileadmin/user_upload/_library/publications/ce/otherreports/090330_UCTE_FrequencyInvestigationReport_Abstract.pdf [accessed January 25, 2019].

[18] Wang Q, Li T, Yang P. Analysis of impact of "strong DC and weak *AC*" on receiving-end power system. IOP Conf Ser: Earth Environ Sci 2018;113:012210. https://doi.org/10.1088/1755-1315/113/1/012210.

[19] Kabalan M, Singh P. Exploring the effect of grid impedance on the large signal stability of an inverter using Lyapunov functions. 2015 North American power symposium (NAPS) 2015. p. 1–6. https://doi.org/10.1109/NAPS.2015.7335106.

[20] Abulanwar Sayed, Weihao Hu, Chen Zhe, Iov Florin. Adaptive voltage control strategy for variable- speed wind turbine connected to a weak network. IET Renewable Power Gener 2015 [accessed December 19, 2018]. https://ieeexplore.ieee.org/stamp/stamp.jsp?tp=&arnumber=7395059.

[21] Almeida PM, Barbosa PG, Oliveira JG, Duarte JL, Ribeiro PF. Digital proportional multi-resonant current controller for improving grid-connected photovoltaic systems. Renewable Energy 2015;76:662–9. https://doi.org/10.1016/j.renene.2014.11.087.

[22] Zhao S, Li R, Gao B, Wang N, Zhang X. Subsynchronous oscillation of PV plants integrated to weak *AC* networks. IET Renew Power Gener 2019;13:409–17. https://doi.org/10.1049/iet-rpg.2018.5659.

[23] Larrode MH, Temez ÍV, Recio SC, Mugica MS, Lopez PE. Integral control of a Multi-Terminal HVDC-VSC transmission system. 2017 Twelfth international conference on ecological vehicles and renewable energies (EVER). IEEE; 2017. p. 1–15.

[24] Haro-Larrode M, Santos-Mugica M, Etxegarai A, Eguia P. Integration of offshore wind energy into an island grid by means of a multi-terminal VSC-HVDC network. 2018 Thirteenth international conference on ecological vehicles and renewable energies (EVER) 2018. p. 1–6. https://doi.org/10.1109/EVER.2018.8362339.

[25] Li G, Du Z, An T, Xia Y, Lei J. Impact of PLL and VSC control parameters on the *AC*/MTDC systems stability. Electr Power Syst Res 2016;141:476–86. https://doi.org/10.1016/j.epsr.2016.08.030.

[26] ENTSO-E. Frequency Sensitive Mode-ENTSO-E guidance document for national implementation for network codes on grid connection; 2017. https://consultations.entsoe.eu/system-development/entso-e-connection-codes-implementation-guidance-d-4/user_uploads/1—igd-on-fsm.pdf [accessed December 11, 2018].

[27] ENTSO-E (European Network of Transmission System Operators for Electricity). Network code for requirements for grid connection applicable to all generators (RfG); 2013. https://www.entsoe.eu/major-projects/network-code-development/requirements-for-generators/.

[28] Khatir M, Zidi SA, Fellah MK, Hadjeri S, Dahou O. HVDC transmission line models for steady-state and transients analysis in SIMULINK environment. IECON 2006 – 32nd annual conference on IEEE industrial electronics Paris: IEEE; 2006. p. 436–41. https://doi.org/10.1109/IECON.2006.347234.

[29] Harnefors L. Modeling of three-phase dynamic systems using complex transfer functions and transfer matrices. IEEE Trans Ind Electron 2007;54:2239–48. https://doi.org/10.1109/TIE.2007.894769.

[30] Alsseid AM, Jovcic D, Starkey A. Small signal modelling and stability analysis of multiterminal VSC-HVDC. Proceedings of the 2011 14th European conference on power electronics and applications. 2011. p. 1–10https://ieeexplore.ieee.org/stamp/stamp.jsp?tp=&arnumber=6020578.

[31] Neumann T, Feltes C, Erlich I. Response of DFG-based wind farms operating on weak grids to voltage sags. 2011 IEEE power and energy society general meeting 2011. p. 1–6. https://doi.org/10.1109/PES.2011.6039565.

[32] Mali Shrikant, James Steffy, Tank Ishwari. Improving low voltage ride-through capabilities for grid connected wind turbine generator. 4th International conference on advances in energy research 2013, ICAER 2013 2013. https://doi.org/10.1016/j.egypro.2014.07.294.